

MAPPING LANDSLIDE SURFACE FISSURES WITH MATCHED FILTERING AND OBJECT-ORIENTED IMAGE ANALYSIS

André Stumpf^{a, b, c, *}, Jean-Philippe Malet^b, Norman Kerle^c

^a Laboratoire Image, Ville, Environnement, CNRS ERL 7230, Université de Strasbourg, 3 rue de l'Argonne, F- 67083 Strasbourg, France

^b Institut de Physique du Globe de Strasbourg, CNRS UMR 7516, Université de Strasbourg / EOST, 5 rue René Descartes, F-67084 Strasbourg, France

^c ITC-Faculty of Geo-Information Science and Earth Observation, University of Twente, Department of Earth Systems Analysis, Hengelosestraat 99, P.O. Box 6, Enschede, 7500 AA, The Netherlands

andre.stumpf[at]unistra.fr
jeanphilippe.malet[at]unistra.fr
kerle[at]itc.nl

KEY WORDS: line detection, crack detection, Gaussian matched filter, object-oriented image analysis, landslide surface fissures, unmanned aerial vehicle

ABSTRACT: Surface fractures are important indicators for geomechanical processes and mapping and monitoring of landslide surface fissures provide valuable information about the slope activity and related hazards. Mappings of surface fissures are traditionally carried out during field surveys, whereas recently aerial photography with sufficient spatial resolution to picture such fine structures is becoming more commonly available. This study targeted the development of a semi-automatic image processing chain to efficiently extract fissure maps from very-high resolution aerial images recorded at the Super Sauze landslide in the Southern French Alps. The developed processing chain combines a Gaussian filters, morphological operators and object-oriented image analysis to exploit higher level scene context. The technique was tested with a heterogeneous set of multi-temporal images recorded at five different dates and the resulting maps were compared quantitatively with expert maps based on field surveys and image interpretation.

1. INTRODUCTION

Fissures at the surface of natural and artificial slopes are elementary geomorphological forms whose spatial extent and fundamental properties (characteristic length, density, and typology) are helpful to interpret slope activity. Mapping their dynamics provides valuable information for the understanding of the mechanical processes of a potential or active landslide (Krauskopf et al., 1939; Ter-Stephanian, 1946; Fleming and Johnson, 1989; Walter et al., 2009) as they represent the first signs of slope instability (Petley et al., 2002). Surface fissures also have considerable effect on the slope hydrology by controlling the infiltration rates of rainfall, and the drainage patterns of local groundwater tables (van Beek and van Asch, 1999; Malet et al., 2005a). From the increasing availability of sub-decimetres images from unmanned aerial vehicles (UAVs) and other aerial survey platforms arises the possibility to detect and map such features using remote sensing (Niethammer et al., 2011). Although, the detection and extraction of linear features is a fundamental operation in digital image processing (Quackenbush, 2004; Mendonca and Campilho, 2006; Papari and Petkov, 2011) relatively few studies have explored the application of automatic approaches for the mapping of geomorphological relevant linear features (Baruch and Filin, 2011; Shruthi et al., 2011). Therefore, it remains challenging to automatically 1) delineate and classify the features to construct multi-temporal fissure maps, and 2) track changes in their spatial pattern to identify trends in the kinematic regime of the landslide.

This work presents the development of a semi-automatic workflow combining line detection (based on Gaussian matched filters), morphological operators and object-oriented image analysis for the detection and mapping of surface fissures. To

assess the performance of the automatic workflow results are compared with manual mappings based on image interpretation and field work.

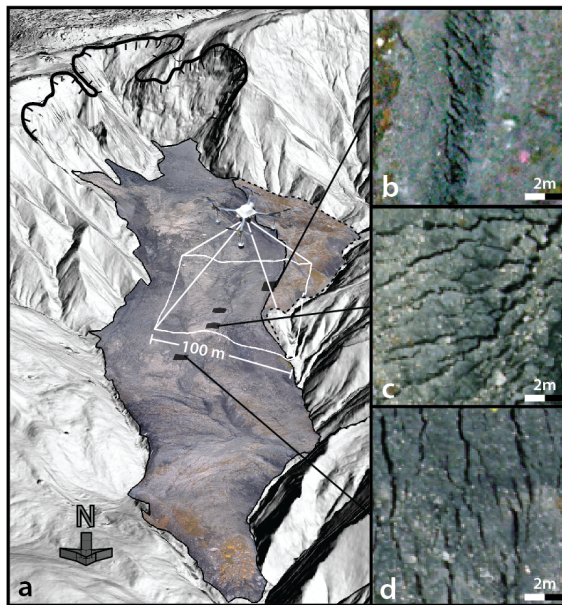


Fig. 1 (a) Oblique view on the Super-Sauze mudslide and (b-d) typical fissure patterns observable in the UAV images.

2. STUDY SITE AND DATA

The study site is the Super-Sauze mudslide located in the Barcelonnette Basin in the South French Alps. It is a complex landslide that has developed in clay-rich black marls, and is

* corresponding author

characterized by very variable displacement rates in space and time. In May 2007 and July 2009, two orthomosaics of optical images with full coverage of the landslide were recorded by private data providers using medium format cameras mounted on an airplane and a helicopter, respectively. In July 2008, October 2008, and October 2009 a low-costs UAV system equipped with compact camera was operated at flight heights between 100 m and 250 m yielding images of the surface with a ground resolution between 0.03 m and 0.1 m. The individual images were corrected for barrel lens distortion, rectified according to ground control points and merged into one large orthomosaic. For further details on the image acquisition and processing the reader is referred to Niethammer et al. (2011). The aerial images have sub-decimetres resolution (Table 1) and allow to identify an abundant occurrence of surface fissures (Fig. 1) spatially distributed over the landslide. Their spatial patterns signal different deformation mechanisms of the landslide, such as lateral shear, extension and compression.

Table 1: Image resolutions at the five different dates.

| Date | May 2007 | July 2008 | October 2008 | July 2009 | October 2009 |
|----------------|----------|-----------|--------------|-----------|--------------|
| Pixel size [m] | 0.10 | 0.10 | 0.08 | 0.05 | 0.05 |

3. METHODS

3.1 Fissure candidate detection with Gaussian filters

A particular well-studied example for the detection of dark curvilinear structures is the extraction of blood vessels in photographs of the human retina. Based on the observation that the cross-profiles of the vessels resembles a Gaussian distribution, Chaudhuri et al. (1989) proposed the use of a matched filter (MF) that is a Gaussian convolution kernel subtracted by its own mean value. As illustrated in Fig. 2, the cross-sections of surface fissures can be approximated with a Gaussian distribution and a MF scaled to the size of the fissure will give a peak response when crossing the fissure at an angle of approximately 90°. Because the MF still yields errors such as false detections at step edges numerous extensions (Hoover et al., 2000; Sofka and Stewart, 2006) and alternative approaches (Mendonca and Campilho, 2006; Soares et al., 2006) have been developed. Recently, Zhang et al. (2010) proposed modification of the original MF filtering approach integrating a first order derivative of a Gaussian function (FDOG) to locally adapt the thresholds. Compared to other state-of-the-art algorithms their approach provided competitive accuracies while being a computationally efficient and hence easier to apply on the large images resulting from VHR remote sensing.

In this study the approach was adapted and implemented in ENVI-IDL 4.8 (EXELIS) as a first level detection routine for the extraction of fissure candidates. For detailed explanation of the functionality of the Gaussian filtering routine the reader is referred to Stumpf et al. (submitted), whereas here only the basic parameters are described. According to the Gaussian fit obtained from cross-profiles (Fig. 2) on the the smallest observed fissures the filters function was scaled with $\sigma=0.06$ m. In practice σ is expressed in units of pixels and adjusted according to the pixel size of the image. The length of the filter was set to 1 m which corresponds to the typical minimum length of the observed features. A threshold parameter Ct controls the sensitivity of the detection and was set to 3.0, which during a sensitivity analysis on spatial subsets of the images was found to provide a suitable trade of between false negatives and false positives detections.

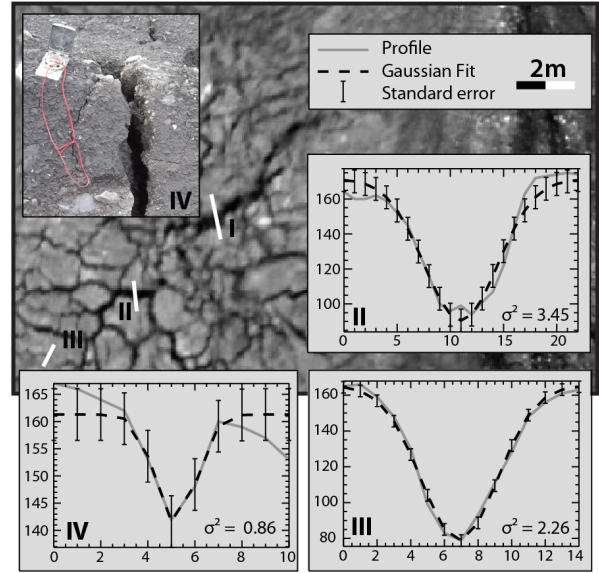


Fig. 2: Typical fissure patterns and (I-III) grey-value profiles (green channel) approximated with Gaussian curves. (IV) Field terrestrial photograph.

3.2 Connection of broken lines using structuring elements

The highly textured surface of the landslide constitutes a noisy background that affects the detection especially at section where the fissures are very thin or partially occluded. While a human operator can easily interpolate broken lines through perceptual grouping (Metzger, 1975), this needs special attention for an automated mapping technique.

To close small gaps between broken line segments of the detected candidates a hit-or-miss transform algorithm (Serra, 1982) was used. The transform assigns a value of 1 to each pixel whose local neighborhood fulfills the criteria defined by hit- and miss structures (Fig. 3a), also known as structuring elements. The hit- and miss-structures were defined to address all plausible 3-by-3 neighborhoods representing small gaps in the detection starting from four prototype hit-structures shown in Fig. 3b. The respective miss-structures are derived by simply inverting the prototype hit-structures, and both elements were rotated to test for a total number of 24 possible neighborhood arrangements. For the structuring elements for closing diagonal gaps an extended neighborhood was used in the miss-structure to prevent connections of parallel lines (Fig. 3b).

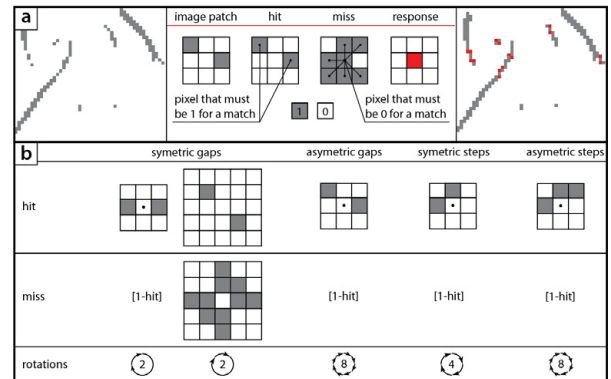


Fig. 3: Strategy used to connect broken line segments. (a) Working principle of the hit- and miss transform and (b) structuring elements for the plausible pixel neighbourhoods.

3.3 Object-oriented analysis for false positive removal

Due to visually similar objects such as linear erosion features (rills, small gullies) and elongated shadows induced by the micro-topography the results of the filtering routine may still comprise numerous false positive candidates. While a human interpreter can differentiate most of the false positives assessing the geospatial context of the scene, the efficient use of such information with automated systems is a challenge for object-oriented image analysis. To exploit the contextual scene information for an automatized refinement of the extracted fissure candidate maps, an object-oriented routine that integrates spatial reasoning into an explicit form was elaborated and implemented using eCognition 8.64 (Trimble, 2011). The elaborated routine included the following steps:

1) The ratio of shadow in the smallest enclosing circle around each candidate is evaluated and candidates with a ratio above 33% are regarded as false detections induced by shadings of the micro-topography. The threshold for shadow was thereby adjusted according to the illumination conditions and the dynamic range of the image (Table 2).

Table 2: Summary of the thresholds adopted in the object-oriented analysis. See text for details.

| Feature | Thresholds |
|---------------------------------|--------------------------|
| Shadows | Red < 100*, 40** |
| Shadow ratio | ≤ 0.33 |
| Vegetation | Ratio blue ≤ 0.33 + Otsu |
| Rel. border to vegetation | ≤ 0.15 |
| Min. angular difference | > 13° |
| Min. length (clean up) | ≥ 0.4 m |
| Min. area (clean up) | > 0.1 m ² |
| Min. fissure density (clean up) | > 1%/10 m ² |

* for May 2007, July 2008 and October 2008

** for July 2009 and October 2009

2) Further false detections may result from vegetation which typically shows a lower reflectance in the green and red channel compared to the blue. The blue ratio in the sum of all channels is consequently typically below one third for vegetated areas. The suitable value varies slightly with the illumination conditions and the season, and Otsu's method (Otsu, 1979) was employed to automatically adapt to such changes. Through an iterative testing of all possible values Otsu's method determines threshold value that maximizes variance between two classes in an image. Hence, constraining the search space to all pixels with a ratio blue below 33% the algorithm was used to determine the thresholds that maximize the contrast between vegetation and the background (Fig. 4). Fissure candidates covered by the resulting vegetation class, or having a relative border length larger than 0.15 were subsequently removed.

3) Another class of false detections resulted from linear objects such as rills, gullies and nearly vertical steps at the landslide flanks, which may locally obtain similar characteristics as the targeted fissures. To test for the presence of larger linear features and evaluate their relationship with fissure candidates, a strategy to suppress additional false positives was required. For the mapping of the larger linear elements two sources were adopted. First drainage lines were extracted from the LiDAR DTMs using hydrological standard tools (Tarboton et al., 1991) and enlarged with a surrounding buffer of 0.5 m. A second approach was to repeat the Gaussian filtering with the parameter set described above, but with a two times increased scale σ and a 5 times coarser image resolution.

Resampling to the coarser resolution was performed with a bilinear interpolation scheme. The linear objects extracted with both approaches were virtually overlaid with the fissure candidates, and the difference of the orientations of their respective center lines was adopted as a criterion to evaluate if the fissure candidate was in fact part of a larger linear object or constitutes an independent structure (Fig. 5). Image-based measurements of the angular offset of the fissured indicated a minimum offset of about $\pm 13^\circ$. Considering that the lowest effective friction angles measured for the landslide material are $\phi' = 26^\circ$ (Malet et al., 2005a), the threshold are consistent with the orientation of $\phi'/2$ that the Coulomb criterion predicts for the orientation of shear fissures at the landslide boundary (Tchalenko, 1970).

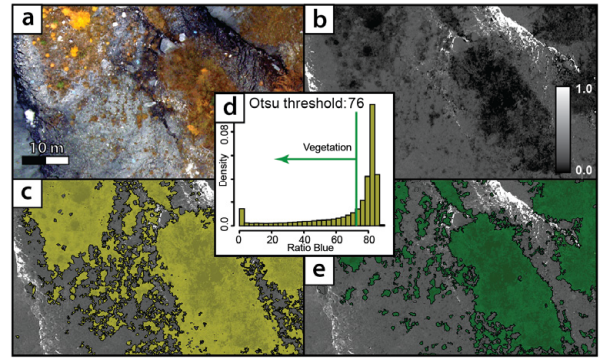


Fig. 4: Automatic threshold detection for the intermediate mapping of vegetation. (a) Subset of the October 2008 image at the toe of the landslide. (b) Ratio blue. (c) Initial thresholding at ratio blue < 0.33 to obtain vegetation candidates (yellow). (d) Histogram of the vegetation candidates with the automatically selected threshold. (e) Final map of the vegetation (green).

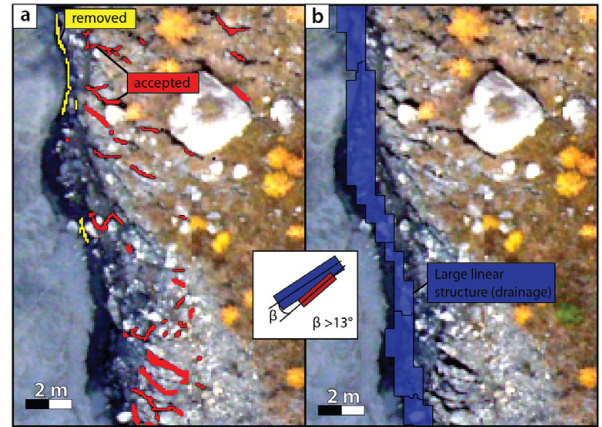


Fig. 5: Illustration of the object-oriented routine to remove false positives induced by larger linear structures. (a) Fissure candidates that overlapped with linear structures. (b) Linear structure detected at a ten times greater filter scale. The fissure candidates aligned with the linear structures at angles below $\pm 13^\circ$ were removed.

4) A last filtering step was implemented removing all candidates with length not longer than 0.4 m and an area smaller than 0.1 m². Finally all fissure candidates falling in areas with a fissure class density lower than 1% in a surrounding neighbourhood of 10 m² were considered as noise and also removed.

4. RESULTS

The primary output of the developed processing routine is a map of the detected fissures represented by polygons. Applying a Delauny triangulation that extracts the skeleton of those polygons (Trimble, 2011) a 2D line representation, which enables a more immediate comparison with expert mappings, can be obtained.

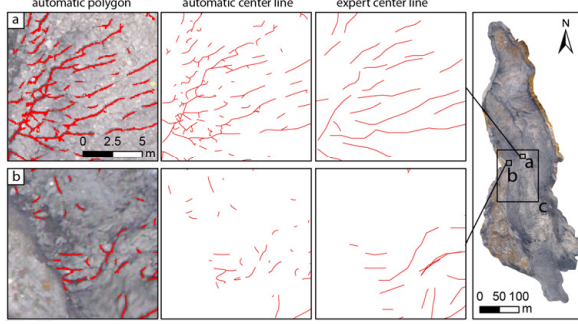


Fig. 6: Exemplary comparison of the obtained fissure maps with the expert mapping for October 2009 (fissures in red). (a) Area with relatively high agreement of the mapped fissure patterns. (b) Area with relatively high rate of false negatives and false positives. (c) Test area. The scale of the representations corresponds approximately to the scale used for the expert mapping (1:250).

Fig. 6 displays exemplarily a comparison between an expert map and the corresponding result of the automatic detection. A first visual assessment of the obtained maps suggested better agreement of the fissure patterns in areas with high contrast and low texture (Fig. 6a), whereas false positives and false negatives concentrated in sections with low contrast and increased surface texture (Fig. 6b).

For a quantitative assessment of the mapping accuracy the obtained results were compared with the expert mappings at the central part of the landslide (Fig. 6c) at all five dates. While several accuracy measures for geographic line datasets have been already proposed, there is still no consensus about one generally applicable technique and the metrics should be selected according to the problem at hand (Ariza-López and Mozas-Calvache, 2012). Here we focused on three crucial aspects of the map accuracy that may have direct implications for their further use, namely the size of the fissured area, the length and density of the fissures, and their orientation.

4.1 Size of the affected area

Tveite and Langaas (1999) suggested an accuracy measure for line datasets based on repeated buffering and overlay operations of both, detected and reference line datasets. A similar strategy was adopted in this study by repeatedly calculating true positive and false positives rates from two raster representing the detections and the expert mapping at increasingly coarser resolutions. Raster were calculated at 10 cm steps for resolutions between 0.10 m and 1.00 m, and each pixel was assigned as fissured or non-fissured area according to the presence of a fissure in the detections and the reference map, respectively. The resulting receiver operating characteristics (ROC) plots of the best and the worst obtained results are presented in Fig. 7. The analysis showed a correspondence with the expert maps at true positive rates typically above 40 % and up to 65%. The false positive rates were below 5% except for the scenes recorded with full sunlight at the surface where false positive rates up to 9% could be observed (Fig. 7a).

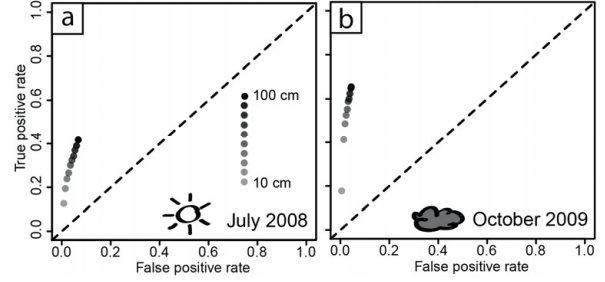


Fig. 7: Receiver operating characteristics (ROC) plots of the fissured area at different map resolutions for (a) the worst results and (b) the best results. The sky conditions for the different dates are indicated.

4.2 Fissure length and density

Hydrological models that integrate the influence of surface fissures on infiltration and preferential flow have demonstrated that the fraction of fissures per unit area is an important parameter with considerable influence on the modeled water storage (Malet et al., 2005b). Such models are typically generated at slope scale with grid resolutions below 10 m. To assess the accuracy of the extracted maps with respect to this potential application the fissure density was calculated as the line length in circular sliding windows with diameters between 2 and 10 m, and compared among automated detection and expert mappings. The regression plots in Fig. 8 illustrate the correlation of the fissure density estimates with a 5 m circular sliding window. The regression analysis indicated generally higher densities resulting from false positive detections of the automatic detection but also from a stronger generalization of the fissure line drawings within the expert mapping.

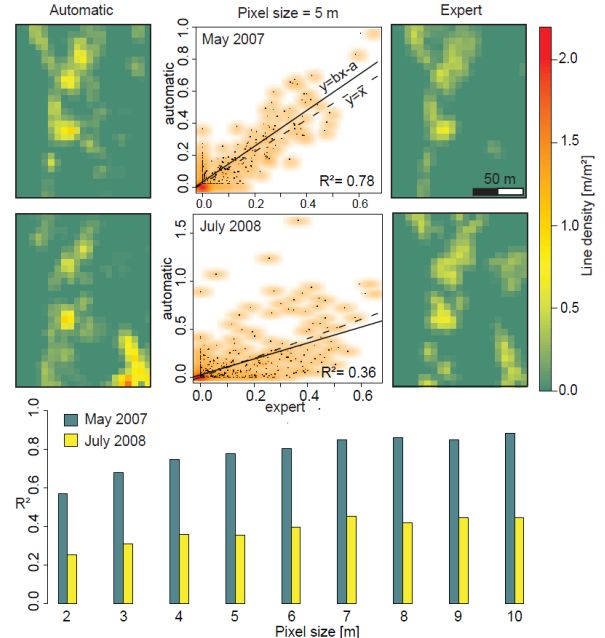


Fig. 8: Strongest and weakest correlation of the fissure densities from automatic detections and expert mappings at 5 m raster resolution. The bar plots at the bottom display the R^2 coefficient at different raster resolutions.

The correlation of the fissure densities was characterized by a coefficient of determination (R^2) typically above 0.5. An exception was the mapping obtained from the image of July

2008 which was recorded at a low sun incidence angle leading to a relatively low $R^2 = 0.36$.

The bar plots in Fig. 8 display the generally higher R^2 values at increasing resolutions of the density raster. This is a well-known effect of spatial aggregation on correlation statistics (Gotway and Young, 2002) but also reflects the contrast between stronger discrepancies of local details and a better correspondence of the global fissure pattern pictured in the respective maps. The highest correlation was observed among the mappings for May 2007 with an $R^2 = 0.88$ at 10 m resolution.

4.3 Fissure orientation

Different fissure patterns may signal respective mechanical processes and statistics of the principal fracture orientation often allow to estimate the directions of the principal stresses involved in their formation (Pollard and Fletcher, 2005). The fissure orientations were therefore quantified as a third factor to assess the accuracy of the extracted maps using rose diagrams frequently employed for the analysis and interpretation of two dimensional orientation data. Rose diagrams with a bin width of 10° were computed on a 10 m regular grid for the automatic detections and the expert mappings at all five dates.

Taking into account all cells containing fissures in both the expert map and the automatic detection the mean absolute error (MAE) of the mean orientations provides a quantitative measure for the orientation accuracy. The rose diagrams plots and error statistics in Fig. 9 depict MAEs between 9.7° and 22.5° as the best and worst results among the five analyzed dates. The detections on the three scenes recorded under cloudy sky resulted in MAE not larger than 10.7° , whereas the error rate clearly exceeded 20° with the scenes of July 2008 and 2009 recorded with full sunlight at the surface. The lower orientation accuracies are largely consistent with the relatively low accuracies in terms of area and density resulting from the detection at the latter two dates.

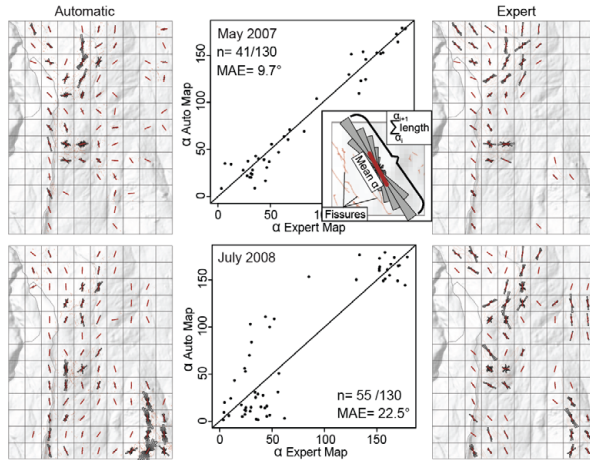


Fig. 9: Rose diagram plots for the best and worst mapping results with mean orientation (red line) and error statistics for the mean fissure orientation per 10 m grid cell for the test area. For visualization, the rose diagrams were plotted over a hillshade of the landslide surface and the scatterplot angles were centred at 90° .

5. DISCUSSION

While Sowers and Royster (1978) argued that aerial photographs do not provide sufficient resolution for detailed mappings of surface fractures, modern digital sensors and new aerial platforms such as UAVs today provide the necessary level of detail. This study demonstrated the possible use of a

semi-automatic image processing chain for the extraction of surface fissure maps. The accuracy of the method was assessed by comparisons with expert maps and demonstrated heterogeneous areal accuracies with true positive rates of up to 65% and false positive rates generally below 10%. Similarly, the orientation accuracy showed a variable quality of the resulting maps with mean deviations between 9.7° and 22.5° .

The fissure densities derived from both maps displayed significant correlations (R^2 between 0.36-0.78), whereas the automatic detections yielded typically higher density estimates. The best agreement among detection and expert maps was measured for the scene of May 2007 showing that lower resolution does not necessarily yield lower accuracies. Generally lower accuracies were however observed for scenes recorded with full sunlight at the surface in July 2008 and 2009. The worst results were obtained for July 2008 when images were recorded at a relatively low sun incidence angle.

Low-level linear feature detectors based on Gaussian filters yield competitive results in medical image analysis (Zhang et al., 2010), whereas the accuracies achieved with aerial images in this study are still significantly lower. This must be attributed to the generally higher complexity of outdoor scenes and requires additional steps and parameters to take the contextual scene information into account. The use of OOA based heuristics proved useful for the removal of false positives, enabled the integration of mechanical laws in the image analysis, and helped objectify the image analysis by transferring expert knowledge in an explicit form. However, the analysis also still relies on a number of empirical fixed thresholds which may hinder an easy transfer of the entire processing chain to a different geographic area. The OOA heuristics already considers multi-scale information to some degree (see 3.33), whereas an explicit integration of an automatic scale selection technique at the low-level filtering stage may appear as a promising approach to further reduce heuristics and tunable parameters.

Despite room for methodological improvements, the obtained fissure maps already provide sufficient detail to infer the landslide dynamics and mechanical processes at the slope scale. Density maps from both automatic and expert mappings picture a strong spatial and temporal variability of the fissure abundance point toward important local and temporal contrasts in the infiltration capacity.

6. CONCLUSION

This study developed an image processing chain to extract surface fissures from heterogeneous sets of VHR aerial images and tested the approach with a challenging multi-temporal set of images recorded at the Super-Sauze landslide for five different dates. The first two stages of the workflow combine families of Gaussian matched filters and morphological operators and are followed by an object-oriented analysis to reduce the amount of false positive detection exploiting contextual information and auxiliary topographic information.

Under homogenous illumination conditions a comparison of the results with expert mappings demonstrated detection rates of up to 65% and orientation errors below 10° . The detection is relatively sensitive to shading effects and prone to errors when applied on images recorded at low sun incidence angles.

Though the processing chain has been specifically designed for the mapping of landslide surface fissures, the first and second stage of the method are generic for the detection of dark linear features and may be applicable to other geomorphological objects with such characteristics. For the mapping of erosion gullies, fault line fractures or ice-glacier crevasses, which

typically exhibit a high contrast to the surrounding homogenous surface, the proposed technique might be of interest. A subsequent object-oriented analysis will typically require adaption to the specific domain and should be useful to explicitly integrate process knowledge in the image analysis chain.

Considering the intrinsic disagreement in expert mappings of linear features, especially in the inter- and extrapolation of lines (Sander et al., 1997), further studies should target to include a general assessment of uncertainties of the expert fissure maps.

References

- Ariza-López, F., Mozas-Calvache, A., 2012. Comparison of four line-based positional assessment methods by means of synthetic data. *Geoinformatica*, 16(2), 221-243.
- Baruch, A., Filin, S., 2011. Detection of gullies in roughly textured terrain using airborne laser scanning data. *ISPRS Journal of Photogrammetry and Remote Sensing*, 66(5), 564-578.
- Chaudhuri, S., Chatterjee, S., Katz, N., Nelson, M., Goldbaum, M., 1989. Detection of blood vessels in retinal images using two-dimensional matched filters. *IEEE Transactions on Medical Imaging*, 8(3), 263-269.
- Fleming, R.W., Johnson, A.M., 1989. Structures associated with strike-slip faults that bound landslide elements. *Engineering Geology*, 27(1-4), 39-114.
- Gotway, C.A., Young, L.J., 2002. Combining Incompatible Spatial Data. *Journal of the American Statistical Association*, 97(458), 632-648.
- Hoover, A.D., Kouznetsova, V., Goldbaum, M., 2000. Locating blood vessels in retinal images by piecewise threshold probing of a matched filter response. *IEEE Transactions on Medical Imaging*, 19(3), 203-210.
- Krauskopf, K.B., Feitler, S., Griggs, A.B., Source, 1939. Structural Features of a Landslide near Gilroy, California. *The Journal of Geology*, 47(6), 630-648.
- Malet, J.P., Laigle, D., Remaitre, A., Maquaire, O., 2005a. Triggering conditions and mobility of debris flows associated to complex earthflows. *Geomorphology*, 66(1-4), 215-235.
- Malet, J.P., van Asch, T.W.J., van Beek, R., Maquaire, O., 2005b. Forecasting the behaviour of complex landslides with a spatially distributed hydrological model. *Natural Hazards and Earth System Sciences*, 5(1), 71-85.
- Mendonca, A.M., Campilho, A., 2006. Segmentation of retinal blood vessels by combining the detection of centerlines and morphological reconstruction. *IEEE Transactions on Medical Imaging*, 25(9), 1200-1213.
- Metzger, W., 1975. *Gesetze des Sehens*, 3. Auflage. Waldemar Kramer, Frankfurt am Main.
- Niethammer, U., James, M.R., Rothmund, S., Travelletti, J., Joswig, M., 2011. UAV-based remote sensing of the Super-Sauze landslide: Evaluation and results. *Engineering Geology*, <http://dx.doi.org/10.1016/j.enggeo.2011.03.012>.
- Otsu, N., 1979. A Threshold Selection Method from Gray-Level Histograms. *IEEE Transactions on Systems, Man and Cybernetics*, 9(1), 62-66.
- Papari, G., Petkov, N., 2011. Edge and line oriented contour detection: State of the art. *Image and Vision Computing*, 29(2-3), 79-103.
- Petley, D.N., Bulmer, M.H., Murphy, W., 2002. Patterns of movement in rotational and translational landslides. *Geology*, 30(8), 719-722.
- Pollard, D.D., Fletcher, R.C., 2005. *Fundamentals of Structural Geology*, Third printing with corrections. Cambridge University Press, New York.
- Quackenbush, L.J., 2004. A review of techniques for extracting linear features from imagery. *Photogrammetric Engineering & Remote Sensing*, 70(12), 1383-1392.
- Sander, P., Minor, T.B., Chesley, M.M., 1997. Ground-Water Exploration Based on Lineament Analysis and Reproducibility Tests. *Ground Water*, 35(5), 888-894.
- Serra, J., 1982. *Image Analysis and Mathematical Morphology*. Academic Press, Orlando, Florida.
- Shruthi, R.B.V., Kerle, N., Jetten, V., 2011. Object-based gully feature extraction using high spatial resolution imagery. *Geomorphology*, 134(3-4), 260-268.
- Soares, J.V.B., Leandro, J.J.G., Cesar, R.M., Jelinek, H.F., Cree, M.J., 2006. Retinal vessel segmentation using the 2-D Gabor wavelet and supervised classification. *IEEE Transactions on Medical Imaging*, 25(9), 1214-1222.
- Sofka, M., Stewart, C.V., 2006. Retinal Vessel Centerline Extraction Using Multiscale Matched Filters, Confidence and Edge Measures. *IEEE Transactions on Medical Imaging*, 25(12), 1531-1546.
- Sowers, G.F., Royster, D.L., 1978. Field Investigation. In: R.L. Schuster, R.J. Krizek (Eds.), *Landslides: Analysis and Control*. Transportation Research Board, Special Report 176, National Academy of Science, Washington, D.C., pp. 81-111.
- Stumpf, A., Malet, J.-P., Kerle, N., Niethammer, U., Rothmund, S., submitted. Image-based mapping of surface fissures for the investigation of landslide dynamics. *Geomorphology*.
- Tarboton, D.G., Bras, R.L., Rodriguez-Iturbe, I., 1991. On the Extraction of Channel Networks from Digital Elevation Data. *Hydrological Processes*, 5, 81-100.
- Tchalenko, J.S., 1970. Similarities between Shear Zones of Different Magnitudes. *Geological Society of America Bulletin*, 81(6), 1625-1640.
- Ter-Stephanian, G., 1946. On the landslide cracks classification. *Bulletin of the Academy of Sciences of the Armenian SSR*, 10, 65-80 (in Russian with abstracts in Armenian and English).
- Trimble, 2011. *eCognition Developer 8.64.0 Reference Book*. Trimble Documentation, München.
- Tveite, H., Langaas, S., 1999. An accuracy assessment method for geographical line data sets based on buffering. *International Journal of Geographical Information Science*, 13(1), 27-47.
- van Beek, L., van Asch, T., 1999. A combined conceptual model for the effects of fissure-induced infiltration on slope stability. In: S. Hergarten, H. Neugebauer (Eds.), *Process Modelling and Landform Evolution. Lecture Notes in Earth Sciences*. Springer Berlin / Heidelberg, pp. 147-167.
- Walter, M., Niethammer, U., Rothmund, S., Joswig, M., 2009. Joint analysis of the Super-Sauze (French Alps) mudslide by nanoseismic monitoring and UAV-based remote sensing. *first break*, 27(8), 53-60.
- Zhang, B., Zhang, L., Zhang, L., Karray, F., 2010. Retinal vessel extraction by matched filter with first-order derivative of Gaussian. *Computers in Biology and Medicine*, 40(4), 438-445.